A Continuum Mechanics Model of Myosin II–Driven Mesodermal Flow in Zebrafish Gastrulation

Carys Garvey*
Department of Physics and Department of Mathematics, California Lutheran University, Thousand Oaks, CA, USA and Department of Physics, University of California Santa Barbara, Santa Barbara, CA, USA

Dr. Sebastian Streichan,† Pieter Derksen,‡ and Dr. Susie Wopat§
Department of Physics, University of California Santa Barbara, Santa Barbara, CA, USA
(Dated: October 1, 2025)

The vertebrate body plan emerges during gastrulation, when coordinated cell flows establish the embryonic axis and generate the three germ layers: endoderm, mesoderm, and ectoderm. While genetic regulation of gastrulation is well studied, the physical mechanisms underlying the coordinated tissue flows remain poorly understood. In zebrafish, mesodermal convergence toward the dorsal side is central to body axis formation, and we hypothesize that localized actomyosin contractility provides the driving force. Here we develop a continuum mechanics framework that links spatial patterns of myosin II activity to mesodermal flows. Using active gel theory, we construct a minimal 1D-flow model in which the mesoderm is treated as a compressible active viscous fluid. The model predicts convergence toward myosin-rich regions, consistent with midline formation. Extending the model to multiple contractile domains predicts that a dorsal–ventral pair of peaks produces dual axes, while clustered peaks on the dorsal side strengthen convergence without creating new axes. These results recapitulate features of classic organizer transplantation experiments and show how complex developmental flows can arise from simple physical principles.

I. INTRODUCTION

Gastrulation is a fundamental stage of vertebrate development during which coordinated cell movements generate the three germ layers—endoderm, mesoderm, and ectoderm—and establish the embryonic body axis [1]. These large-scale rearrangements set the stage for organogenesis and ultimately define the body plan. While the molecular signaling pathways underlying gastrulation have been extensively characterized, the physical mechanisms that drive tissue-scale flows remain less well understood. In this work, we develop a mechanical model to investigate how mesodermal flows arise during zebrafish gastrulation.

The zebrafish embryo provides a powerful system to study gastrulation mechanics, owing to its optical accessibility and well-defined developmental timeline. Light-sheet imaging has revealed global flow patterns, with the mesoderm in particular exhibiting stationary dual-vortex structures and convergence toward the midline—features that highlight its central role in gastrulation mechanics. While imaging has mapped these mesodermal kinematics, the underlying force-generating mechanisms remain unclear. Actomyosin contractility is a strong candidate, as it drives morphogenetic motion in diverse systems [2], but whether spatial distributions of myosin II are sufficient to account for mesodermal convergence in zebrafish remains an open question.

Here, we develop a continuum mechanics framework to explore how myosin contractility shapes mesodermal flow during zebrafish gastrulation. Using active gel theory, we construct a 1D-flow model in which the mesoderm is treated as a compressible active viscous fluid. This minimal framework yields analytic solutions that link spatial asymmetries in contractility to convergent flow. We then extend the model to scenarios with multiple contractile domains, enabling comparison to classic organizer transplantation experiments [3]. Together, these results demonstrate how complex developmental flows can emerge from simple physical rules, providing a quantitative link between molecular-scale force generation and tissue-scale morphogenesis.

II. BACKGROUND

A. Zebrafish Gastrulation

In zebrafish (*Danio rerio*), gastrulation begins around 5 hours post-fertilization (hpf) and proceeds until formation of the tailbud at approximately 10 hpf [1]. During this period, cells atop the spherical yolk cell undergo spreading, folding, and coordinated rearrangements that establish the embryonic body axis. This process is visualized in Figure 1.

A central outcome of these cell rearrangements is the formation of the three germ layers: endoderm, mesoderm, and ectoderm. The endoderm, the innermost layer, ultimately gives rise to the gut and associated organs. The ectoderm, the outer layer, develops into the

* cgarvey@callutheran.edu
† streicha@physics.ucsb.edu
‡ pieterderksen@ucsb.edu
§ wopat@ucsb.edu

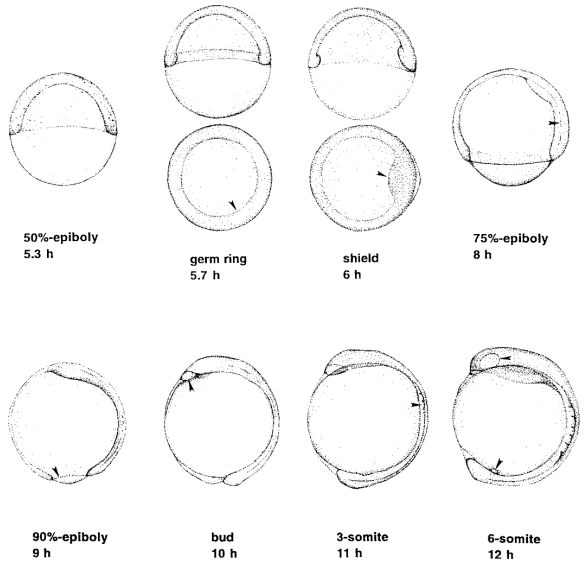

FIG. 1. Key stages of zebrafish gastrulation (adapted from Kimmel *et al.* [1]). Between 5–10 hours post fertilization (hpf), cells undergo coordinated morphogenetic movements: epiboly (cell layers spreading over the yolk, 5–10 hpf), involution at the margin to generate mesoderm and endoderm (6 hpf), and dorsal accumulation of cells to establish the embryonic shield (6 hpf). Epiboly ends with formation of the tail bud, where the embryo then enters the somite stage, during which segmented somites form along the body axis. Arrows indicate the embryonic shield and other morphological landmarks at each stage.

epidermis and nervous system. The mesoderm, positioned between them, plays a key role in gastrulation. In addition to forming muscles, the skeleton, and many internal organs, the mesoderm undergoes large-scale collective flows that contribute directly to axis formation. Recent quantitative imaging has shown that mesodermal convergence and extension are central to shaping the embryonic body plan [4–6].

At the tissue scale, convergent mesodermal flows are essential for midline formation. While the underlying cellular mechanisms remain an active area of study, actomyosin networks are strong candidates for producing the contractile stresses that drive these flows. Studies have shown that global myosin II distribution is linked to tension asymmetries during gastrulation in both the zebrafish and other species [2, 7]. To place these findings in context, we next review the role of myosin II in generating cellular contractility.

B. Myosin II as a Driver of Contractility

Myosin II is a molecular motor that generates forces in the actin cytoskeleton of cells by converting chemical energy from ATP into mechanical work. It slides actin filaments relative to one another, producing contractile

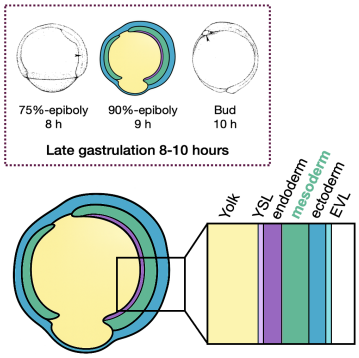

FIG. 2. Cross-sectional view of a zebrafish embryo during late gastrulation (around 90% epiboly). The schematic highlights the yolk, yolk syncytial layer (YSL), the three germ layers (endoderm, mesoderm, and ectoderm), and the outer enveloping layer (EVL). The top panel shows where this stage falls in Kimmel's developmental timeline [1].

stress.

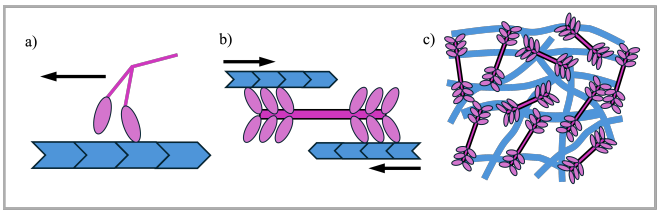

FIG. 3. (a) A non-muscle myosin II motor walking along an actin filament. (b) Myosin motors can assemble into bipolar mini-filaments, generating contractile forces on actin filaments. (c) At the tissue scale, many such motors collectively produce anisotropic active stresses within the actomyosin meshwork, which can drive large-scale cellular flows. Adapted from [8].

At the cellular level, this actomyosin contractility underlies processes such as cytokinesis, migration, and adhesion [8]. At the tissue scale, coordinated myosin activity generates contractile stresses that drive collective flows and large-scale morphogenesis [2]. A key feature is that the net contractile behavior depends not only on the activity of myosin itself but also on the organization of actin filaments. Aligned filaments bias microscopic motor activity toward global contraction, whereas disordered networks may balance contractile and extensile forces [8]. Studies have shown that the spatial distribution and orientation of myosin motors are predictive of where and how tissues deform during development [2], a relationship often formalized within the framework of active gel theory.

C. Active Gel Theory for Myosin II–Generated Stress

To bridge molecular-scale activity with tissue-scale mechanics, theoretical approaches often use active gel theory. In this framework, the actomyosin network is modeled as a compressible active viscoelastic medium with an internal stress proportional to the local myosin density [8]. Even though the actomyosin network is complex at the molecular level, coarse-grained continuum models with a small number of parameters have been surprisingly effective at reproducing tissue-scale behavior [2].

In practice, the active stress can be written as

$$\sigma_{ij}^{\text{active}} = \zeta_a m_{ij}, \tag{1}$$

where ζ_a represents the magnitude of myosin-generated tension and m_{ij} is a nematic orientation tensor [9]. This level of description has successfully connected microscopic actomyosin dynamics to continuum mechanics of epithelial sheets and embryonic tissues. For instance, in *Drosophila*, measured myosin distributions are sufficient to predict gastrulation flow fields [2]. Whether a similar quantitative relationship applies in zebrafish remains an open question, motivating our present work.

D. Material Properties and Modeling Assumptions

When applying active gel concepts to zebrafish mesodermal movements in gastrulation, it is important to consider the effective material properties of the mesoderm. Experimental work has shown that posterior mesodermal tissues behave more like viscous fluids than elastic solids, as stress fluctuations on minute timescales allow rapid rearrangements that fluidize the tissue [10]. Guided by these insights, we describe the mesoderm as a viscous active fluid with contractile stress proportional to myosin distribution. This minimal continuum framework links spatial patterns of myosin activity to emergent flow fields and forms the basis for our model.

III. METHODOLOGY

In this section, we outline the modeling framework used to connect mesodermal myosin activity to large-scale tissue flows. We begin with a minimal analytic 1D-flow model, which treats the mesoderm as a compressible active viscous fluid.

A. Model Geometry

During gastrulation, mesodermal cells involute at the margin and spread as a circumferential band around the equator of the yolk cell. To capture this organization in a minimal setting, we represent the mesoderm as a band near the equator of the spherical yolk cell. This geometry is projected into a planar two-dimensional strip with periodic boundary conditions in the azimuthal (ϕ) direction (Fig. 4). Within this strip, we focus on flow along ϕ. Here ϕ is the azimuthal angle (dimensionless). For analytical tractability, we nondimensionalize length by the embryo radius R, effectively setting $R = 1$ in our derivations. This simplification reduces algebraic complexity without sacrificing generality, as physical quantities can be recovered by reintroducing R in the final expressions. These assumptions capture the essential convergent mechanics generated by localized contractility while providing a minimal setting for analytic solutions.

B. Constitutive Equations

We model the mesoderm's material properties as a compressible active viscous fluid characterized by bulk viscosity η_b, shear viscosity η_s, and contractile activity ζ_a. Following the formulation of Behrndt *et al.* [7], the total stress tensor is

$$\sigma_{ij} = \eta_b(\partial_k v_k)\delta_{ij} + \eta_s\big(\partial_i v_j + \partial_j v_i - (\partial_k v_k)\delta_{ij}\big) + \zeta_a m_{ij} \tag{2}$$

where v_i is the velocity field, δ_{ij} is the Kronecker delta, and m_{ij} is the myosin orientation tensor.

Although individual cells are effectively incompressible, treating the mesoderm as compressible provides a useful coarse-grained approximation. As in the work of Behrndt *et al.* on EVL and YSL spreading during zebrafish gastrulation [7], we allow for effective compressibility at the tissue scale. In this description, apparent area changes reflect local rearrangements, variations in tissue thickness, and exchange of cells with neighboring layers. Representing the mesoderm as a compressible viscous sheet therefore captures large-scale flows while permitting local divergence, yielding a minimal and analytically tractable framework for our model.

Since incompressibility is not enforced, we omit an explicit pressure term. Mechanical equilibrium then requires

$$\partial_j \sigma_{ij} = 0. \tag{3}$$

1. *Anisotropic active stress.*

In active gel theory, filament alignment enters through $m_{ij} = n_i n_j$, where $\mathbf{n}$ is the local filament orientation. Isotropic networks yield $m_{ij} \sim \delta_{ij}$, giving uniform contractile stress [7]. Here we instead assume circumferential alignment, $\mathbf{n} = \hat{\phi}$, giving

$$m_{ij} = \hat{\phi}_i \hat{\phi}_j, \tag{4}$$

so that active stresses project purely along the azimuthal direction. This anisotropic choice is motivated by the presence of supracellular actomyosin cables and aligned contractile structures in other morphogenetic systems [2, 11]. In zebrafish mesoderm, the organization of actomyosin is less well characterized, but as a minimal assumption we impose circumferential alignment to test whether directional contractility alone is sufficient to drive convergence toward the dorsal midline.

2. *Spatial distribution of activity.*

The magnitude of active stress is represented as a Gaussian peak centered at the dorsal side,

$$\zeta_a(\phi) = \zeta_0 \exp\left[-\frac{(\phi-\phi_0)^2}{2\sigma^2}\right], \tag{5}$$

with peak strength ζ_0, center ϕ_0 (dorsal midline), and width σ controlling how localized the enrichment is.

Combining equations 1 and 5, the active stress tensor is therefore

$$\sigma_{ij}^{active} = \zeta_a(\phi) m_{ij} = \zeta_0 \exp\left[-\frac{(\phi-\phi_0)^2}{2\sigma^2}\right] \hat{\phi}_i \hat{\phi}_j \tag{6}$$

3. *Final form.*

Combining viscous and active contributions, the governing equation from Eqn 3 is

$$\partial_j \sigma_{ij}^{\text{viscous}} = -\partial_j \sigma_{ij}^{\text{active}}, \tag{7}$$

with

$$\sigma_{ij}^{\text{viscous}} = \eta_b(\partial_k v_k)\delta_{ij} + \eta_s\left[\partial_i v_j + \partial_j v_i - (\partial_k v_k)\delta_{ij}\right], \tag{8}$$

$$\sigma_{ij}^{\text{active}} = \zeta_a(\phi)\, \hat{\phi}_i \hat{\phi}_j. \tag{9}$$

IV. RESULTS

A. Analytic Solution for Azimuthal Flow

We now solve for the velocity profile of mesodermal flow in the azimuthal direction. The derivation proceeds in three steps: (i) simplifying the stress contributions, (ii) formulating the governing ordinary differential equation (ODE) from force balance, and (iii) solving for $v_\phi(\phi)$ under periodic boundary conditions.

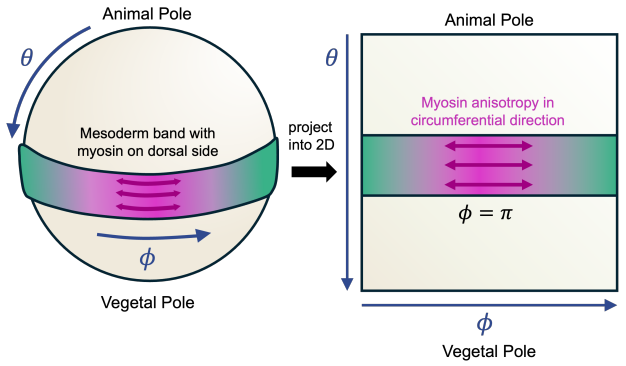

FIG. 4. *Schematic of model geometry and myosin anisotropy.* The mesoderm is represented as a band near the equator of the spherical yolk cell (left), enriched with myosin on the dorsal side. For analysis, this band is projected into a 2D strip with periodic boundaries in the ϕ direction (right). Myosin filaments are assumed to be circumferentially aligned, producing anisotropic contractile stress along ϕ with a Gaussian intensity profile.

1. *Stress contributions*

a. Active stress. Because myosin filaments are assumed circumferentially aligned, the active stress tensor, Eqn 9 reduces to

$$\sigma_{\phi\phi}^{\text{active}} = \zeta_a(\phi), \qquad \sigma_{\theta\theta}^{\text{active}} = \sigma_{\theta\phi}^{\text{active}} = 0. \tag{10}$$

b. Viscous stress. For the viscous part, Eq 8 simplifies considerably. Since $v_\theta = 0$,

$$\sigma_{\phi\phi}^{\text{viscous}} = (\eta_b + \eta_s)\, \partial_\phi v_\phi. \tag{11}$$

c. Force balance. Eqn 3 then reduces to the 1D equation

$$(\eta_b + \eta_s)\, \partial_\phi^2 v_\phi + \partial_\phi \zeta_a(\phi) = 0. \tag{12}$$

2. *Solving the ODE*

Now we can solve the ordinary differential equation (12) by integrating twice to obtain an analytic solution for velocity.

a. First integral. Integrating once gives

$$(\eta_b + \eta_s)\, \partial_\phi v_\phi(\phi) = -\zeta_a(\phi) + C_1, \tag{13}$$

where C_1 is an integration constant.

b. Second integral (general form). A second integration yields

$$v_\phi(\phi) = -\frac{1}{\eta_b+\eta_s}\int \zeta_a(\phi)\,d\phi + \frac{C_1}{\eta_b+\eta_s}\,\phi + C_2, \quad (14)$$

with C_2 another constant determined by boundary conditions.

3. Solving for velocity with Gaussian activity profile for one peak.

Using the Gaussian active stress profile introduced in Eq. (5) defined in Section III, the integral in Eq. (14) becomes

$$\int \zeta_a(\phi)\,d\phi = \zeta_0 \int \exp\left[-\frac{(\phi-\phi_0)^2}{2\sigma^2}\right] d\phi.$$

The standard antiderivative of a Gaussian is given by the error function [12],

$$\int \exp\left[-\frac{(\phi-\phi_0)^2}{2\sigma^2}\right] d\phi = \sigma\sqrt{\frac{\pi}{2}}\,\mathrm{erf}\left(\frac{\phi-\phi_0}{\sqrt{2}\sigma}\right).$$

Therefore,

$$\int \zeta_a(\phi)\,d\phi = \zeta_0\sigma\sqrt{\frac{\pi}{2}}\,\mathrm{erf}\left(\frac{\phi-\phi_0}{\sqrt{2}\sigma}\right).$$

Plugging this into Eq. (14) gives

$$v_\phi(\phi) = -\frac{\zeta_0\sigma}{\eta_b+\eta_s}\sqrt{\frac{\pi}{2}}\,\mathrm{erf}\left(\frac{\phi-\phi_0}{\sqrt{2}\sigma}\right) + \frac{C_1}{\eta_b+\eta_s}\,\phi + C_2.$$

To simplify notation, we define

$$A := \frac{\zeta_0\sigma}{\eta_b+\eta_s}\sqrt{\frac{\pi}{2}}. \quad (15)$$

Thus the velocity profile takes the compact form

$$v_\phi(\phi) = -A\,\mathrm{erf}\left(\frac{\phi-\phi_0}{\sqrt{2}\sigma}\right) + \frac{C_1}{\eta_b+\eta_s}\,\phi + C_2. \quad (16)$$

To fix the integration constants, we now impose physical boundary conditions.

a. Periodic boundary condition. Since the tissue is modeled as a closed band, the velocity must be periodic in ϕ:

$$v_\phi(0) = v_\phi(2\pi). \quad (17)$$

Plugging the general solution (16) into (17) gives

$$\frac{C_1}{\eta_b+\eta_s}\,2\pi = A\left[\mathrm{erf}\left(\frac{2\pi-\phi_0}{\sqrt{2}\sigma}\right) - \mathrm{erf}\left(\frac{-\phi_0}{\sqrt{2}\sigma}\right)\right]. \quad (18)$$

Thus

$$C_1 = \frac{\eta_b+\eta_s}{2\pi}\,A\left[\mathrm{erf}\left(\frac{2\pi-\phi_0}{\sqrt{2}\sigma}\right) - \mathrm{erf}\left(\frac{-\phi_0}{\sqrt{2}\sigma}\right)\right]. \quad (19)$$

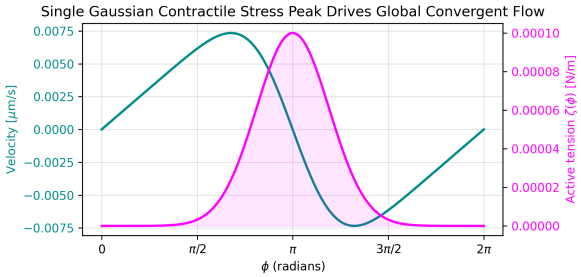

FIG. 5. Predicted azimuthal velocity (teal, [μm/s]) and active stress profile (pink, [N/m]) for a Gaussian myosin distribution centered at $\phi = \pi$. Converted to physical units by reintroducing the embryo radius R. Flow converges toward the contractile region, consistent with experimental observations of dorsal-directed mesodermal flow. Parameters were chosen to reflect realistic biological values [7, 10]: $\zeta_0 = 10^{-4}$ N/m, $\eta_s = 1.0$ N·s/m, $\eta_b = 1.1$ N·s/m (total $\eta = 2.1$), and $R = 350$ μm.

b. Choice of reference frame for C_2. The integration constant C_2 corresponds to a uniform drift of the entire tissue band, reflecting the fact that only velocity differences are physically meaningful. To remove this freedom, we choose a reference frame in which the peak location $\phi = \phi_0$ is stationary:

$$v_\phi(\phi_0) = 0. \quad (20)$$

Substituting Eq. (16) then fixes

$$C_2 = -\frac{C_1}{\eta_b+\eta_s}\,\phi_0. \quad (21)$$

c. Final solution. Combining Eqs. (16), (19), and (21), the closed-form velocity profile is

$$\boxed{v_\phi(\phi) = -A\,\mathrm{erf}\left(\frac{\phi-\phi_0}{\sqrt{2}\sigma}\right) + \frac{C_1}{\eta_b+\eta_s}\,(\phi-\phi_0)} \quad (22)$$

with A given by Eq. (15) and C_1 by Eq. (19).

4. Dorsal peak case.

For $\phi_0 = \pi$ (representing a myosin peak at the dorsal side), the velocity profile is

$$\boxed{v_\phi(\phi) = -A\,\mathrm{erf}\left(\frac{\phi-\pi}{\sqrt{2}\sigma}\right) + \frac{C_1}{\eta_b+\eta_s}\,(\phi-\pi)} \quad (23)$$

5. Multiple Contractile Peaks: Analytic Solution

We now extend the model to cases where the active stress comprises multiple Gaussian peaks. Biologically,

this can represent situations in which several myosin-rich contractile domains coexist along the circumference.

Because the governing 1D balance (Eq. (12)) is linear, the solution for multiple peaks is the superposition of single-peak solutions. Let

$$\zeta_a(\phi) = \sum_{k=1}^{N} \zeta_0^{(k)} \exp\left[-\frac{\left(\phi - \phi_0^{(k)}\right)^2}{2\,\sigma_k^2}\right],$$

with centers $\phi_0^{(k)}$, widths σ_k (radians), and amplitudes $\zeta_0^{(k)}$ (N/m). Then the velocity profile is

$$\boxed{v_\phi(\phi) = -\sum_{k=1}^{N} A^{(k)} \operatorname{erf}\left(\frac{\phi - \phi_0^{(k)}}{\sqrt{2}\,\sigma_k}\right) + \frac{C_1}{\eta_b + \eta_s}\,\phi + C_2} \tag{24}$$

with

$$A^{(k)} = \frac{\zeta_0^{(k)}\,\sigma_k}{\eta_b + \eta_s}\sqrt{\frac{\pi}{2}} \tag{25}$$

Boundary conditions and frame. As in the one-peak case, *a single global pair* (C_1, C_2) applies to the entire superposed profile: periodic boundary conditions fix C_1, and a frame choice fixes C_2 (e.g., zero-mean velocity $\int_0^{2\pi} v_\phi\, d\phi = 0$ or $v_\phi(\phi_*) = 0$ at a reference angle). This ensures uniqueness up to a physically irrelevant constant offset in v_ϕ.

Illustrative scenarios. We consider three representative stress patterns:

- **Dorsal–ventral pair:** two equal peaks at $\phi = 0$ ($\equiv 2\pi$) and $\phi = \pi$ (Fig. 6).
- **Evenly spaced triplet:** three equal peaks at $\phi = 0,\ 2\pi/3,\ 4\pi/3$ (Fig. 7).
- **Dorsal-biased triplet:** three equal peaks localized to the dorsal half, with maxima at $\phi = \pi$ (dorsal midline) and $\phi = \pi/2,\ 3\pi/2$ (Fig. 8).

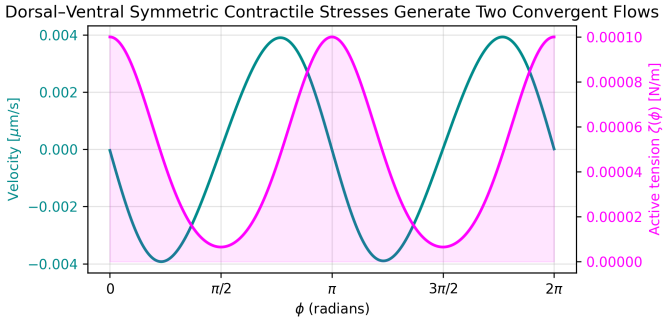

FIG. 6. **Dorsal–ventral two-peak case.** Predicted azimuthal velocity $v_\phi(\phi)$ (teal, [μm/s]) and active tension profile $\zeta_a(\phi)$ (magenta, [N/m]) for two equal Gaussian stress peaks centered at $\phi = 0$ and $\phi = \pi$. The superposed solution yields symmetric convergent flows toward each contractile domain. *Axes:* x is ϕ (radians). Velocities are obtained by solving Eq. (24) for $v_\phi(\phi)$ and restoring physical units by reintroducing R. *Parameters:* $\zeta_0 = 10^{-4}$ N/m (both peaks), $\eta_s = 1.0$ and $\eta_b = 1.1$ N·s/m (total $\eta = 2.1$ N·s/m), $R = 350$ μm.

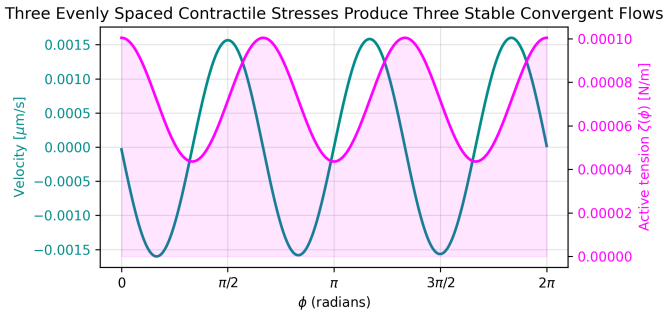

FIG. 7. **Evenly spaced triplet.** Predicted azimuthal linear velocity $v_\phi(\phi)$ (teal, [μm/s]) and active tension $\zeta_a(\phi)$ (magenta, [N/m]) for three equal Gaussians at $\phi = 0,\ 2\pi/3,\ 4\pi/3$. Each contractile domain seeds a local convergence; periodicity enforces a global balance across the three. *Axes/units and conversion:* as in Fig. 6. *Parameters:* $\zeta_0 = 10^{-4}$ N/m (each peak), $\eta = 2.1$ N·s/m ($\eta_s = 1.0$, $\eta_b = 1.1$), $R = 350$ μm.

V. DISCUSSION

A. Converging Flow in the One-Peak Case: Midline Formation

The one-peak model suggests that asymmetric myosin contractility can drive large-scale mesodermal flow toward the dorsal side. This prediction is consistent with biological observations of gastrulation. For example, Fig. 9 shows dorsal accumulation of cells that form the embryonic shield, the first visible marker of the future midline [1]. This shield thickening reflects dorsal-directed convergence, qualitatively aligned with the flows predicted by our model.

Further support comes from velocity fields reconstructed from live imaging (Fig. 10). These flow maps reveal dorsal-directed convergence during gastrulation, consistent with the one-peak model prediction. This qualitative agreement strengthens the link between asymmetric contractility and large-scale convergence.

Future work will integrate measured myosin profiles into the model, extend the framework to fully 3D simulations, and directly compare model predictions with live-imaging flow field reconstructions.

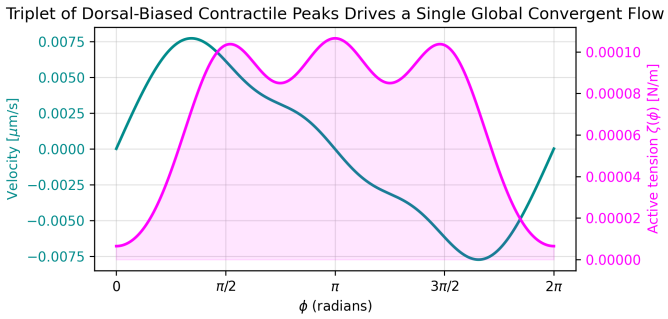

FIG. 8. **Dorsal-biased triplet**. Predicted azimuthal linear velocity $v_\phi(\phi)$ (teal, [μm/s]) and active tension $\zeta_a(\phi)$ (magenta, [N/m]) for three equal Gaussian peaks centered at $\phi = \pi/2$, π, $3\pi/2$ (dorsal half). Superposition merges the individual convergence zones into a stronger net flow toward the dorsal side. *Axes/units and conversion:* as in Fig. 6. *Parameters:* $\zeta_0 = 10^{-4}$ N/m (each peak), $\eta = 2.1$ N·s/m ($\eta_s = 1.0$, $\eta_b = 1.1$), $R = 350$ μm.

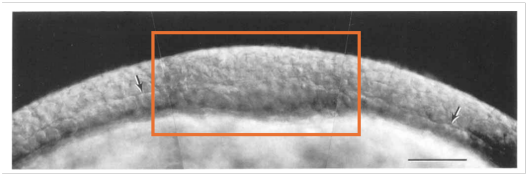

FIG. 9. Dorsal convergence during zebrafish gastrulation (adapted from [1]). Cells accumulate dorsally to form the embryonic shield (boxed), the first visible marker of the midline. Scale bar = 50 μm.

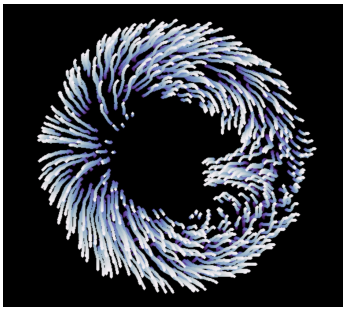

FIG. 10. Experimental trajectories during zebrafish gastrulation, reconstructed from live imaging. Convergent flow toward the dorsal side is evident, qualitatively consistent with the one-peak model prediction of dorsal-directed mesodermal flow. Image Credit: Vishank Jain-Sharma.

B. Converging Flow in Multi-Peak Cases: Relation to Organizer Experiments

1. *Dorsal–ventral symmetry (two peaks).*

For the dorsal–ventral configuration, the model predicts symmetric convergent flows toward both peaks. This behavior is reminiscent of the secondary axis formation observed in the classic Spemann–Mangold organizer transplantation experiments [13], where two sites of organizer activity could induce two axes.

2. *Evenly spaced triplet (three peaks).*

When three contractile stresses are evenly distributed around the circumference, the model predicts three separate convergent flows, each aligned with a peak. This arrangement resembles the induction of multiple organizer-like domains, suggesting that evenly distributed contractile activity could—in principle—support multiple axis initiation events.

3. *Dorsal-clustered triplet (three peaks).*

In contrast, when three peaks are clustered on the dorsal side, the flow fields collapse into a single global convergence toward the dorsal half of the tissue. This is qualitatively similar to cases where organizer tissue transplanted near the endogenous dorsal side results not in multiple axes, but in a broadened or reinforced dorsal organizer domain. The model thus suggests that clustering of contractile domains can amplify dorsal convergence without generating additional axes.

VI. FUTURE ENDEAVORS

This work opens several promising directions for further study, spanning both theoretical refinement and experimental validation.

A. Data-informed modeling

A natural next step is to incorporate experimental measurements of myosin distribution directly into the active stress term of the model. Fluorescence intensity can be used as a proxy for local myosin motor concentration and activity, as previously demonstrated in *Drosophila* gastrulation by Streichan *et. al* [2]. This approach would move the model beyond idealized Gaussian profiles and provide a quantitative link between imaging data and flow predictions.

As part of my work in the Streichan lab this summer, we used antibody staining to visualize cytoskeletal activity within different tissue layers during gastrulation. Specifically, tbx16-eGFP served as a mesodermal tissue marker, while phospho-Myosin (active myosin) was used as a marker of contractile activity.

To process volumetric datasets from the light-sheet microscope, we employed a Blender-based tissue cartography pipeline. This workflow transforms three-dimensional (3D) embryo data into two-dimensional (2D) surface maps, enabling us to isolate individual tissue layers for analysis. One such map is shown below, where

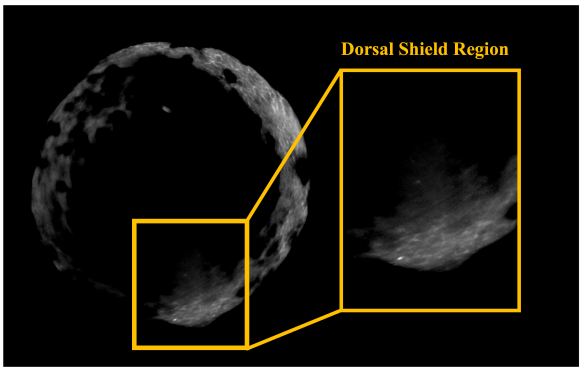

FIG. 11. Maximum-intensity projection of phospho-myosin signal restricted to the mesodermal tissue layer of a zebrafish embryo. The inset highlights the dorsal shield region. Fluorescence intensity serves as a proxy for local myosin motor concentration and actomyosin activity.

Image credit: Carys Garvey, Manxi Zhang, Emily Le.

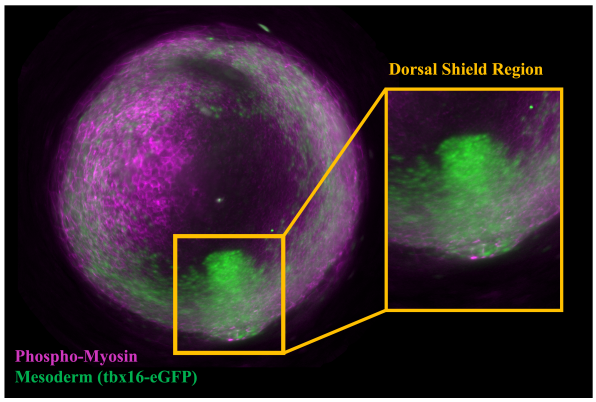

FIG. 12. Multichannel imaging of zebrafish gastrulation. Global myosin (magenta) and mesoderm (green) are shown, with the dorsal shield region highlighted (box). Unexpectedly, myosin signal is weak in the shield itself, with enrichment mainly at its base. This suggests that large-scale mesodermal convergence may arise from contractile activity outside, rather than within, the shield.

Image credit: Carys Garvey, Manxi Zhang, Emily Le.

myosin intensity is represented as a maximum-intensity projection restricted to the mesodermal layer.

A multichannel version of the same dataset further highlights spatial context. Here, global myosin distribution is shown in magenta across the entire embryo, while the mesodermal tissue marker is shown in green.

Our initial experimental results yielded a surprising finding. We observe less myosin in the mesoderm than expected, with very little signal in the dorsal shield region overall.

This unexpected distribution has important implications for our model. The low overall myosin signal suggests either:

- The magnitude of active stress ζ_0 may be lower than our initial estimates
- Other force-generating mechanisms (e.g., cell-cell adhesion or forces from adjacent tissues) may contribute significantly to mesodermal convergence
- The spatial pattern of contractility may be more complex than a simple dorsal peak, potentially involving multiple weak sources that sum to produce net convergence

Future work will require additional imaging and staining across gastrulation stages to fully characterize how myosin II spatial patterns in the mesoderm correlate with convergent flows. This mesoderm-specific analysis is particularly novel, as previous studies have typically examined myosin dynamics in composite tissues rather than isolating this key germ layer. Resolving this quantitative relationship is the crucial next step for testing and refining our mechanical model of mesodermal convergence.

B. Extension to two-dimensional flow

While the present simplified model focuses on circumferential flow, a natural extension is to treat mesodermal motion in two dimensions. Work is already in progress on a finite-element implementation in FEniCSx, which allows evaluation of the weak form of the governing equations to obtain full 2D velocity fields. In this setting, myosin filaments need not be purely circumferentially aligned, and complex anisotropies can be explored. Because current simulations still rely on predicted or preliminary distributions, a continued dialogue between experiment and modeling will be essential.

C. Experimental tests of model predictions

The model also motivates biological experiments that can directly test its predictions. One avenue is transplantation of organizer tissue at varying positions to ask whether there exists a minimum separation required for independent axis formation, or whether closely spaced organizers instead merge into a single convergent domain. While the classic Spemann–Mangold experiments established that transplanted organizers can induce secondary axes, the physical length scales that govern when organizers act independently versus interact remain unknown.

A second avenue is to probe the role of vortical flows. By altering the spatial extent of transplanted tissue, one could test whether there are critical vortex sizes required for stable axis generation. This could help reveal the geometric and mechanical constraints that set the limits of axis formation during gastrulation.

D. Broader implications

This work also raises broader questions about whether similar physical mechanisms are conserved across verte-

brate species. Although different species employ distinct morphogenetic strategies during gastrulation, they exhibit striking similarities in the large-scale cell rearrangements that establish the embryonic axis. Could conserved mechanical principles—perhaps reflecting evolutionary constraints or general energy-minimizing strategies—underlie axis formation across species? This question could be a rich area of exploration in biophysics. Developing a unifying mechanical framework for gastrulation would represent an important step toward connecting molecular force generation with tissue-scale flows, and toward understanding how shared physical rules can give rise to diverse developmental outcomes.

VII. ACKNOWLEDGMENTS

I would like to thank my wonderful mentors, Susie Wopat and Pieter Derksen, for their invaluable guidance and support. I am also grateful to Professor Sebastian Streichan for the opportunity to work in his lab this summer. I especially thank Fridtjof Brauns, Manxi Zhang, Emily Le, and Matthew Lefebvre for their encouragement and many insightful discussions throughout this project.

I also extend my gratitude to the UCSB Physics Department and REU Site Director Sathya Guruswamy for providing this excellent research opportunity. Finally, I am especially grateful for the support and friendship of my fellow REU students—Logan Bennett, Ishan Deb, Lukas Kiekover, Garrett Kunkler, Beto Patino Luna, Seda Peacher, and Rosemary Wynnychenko—who made this experience so rewarding.

This work was supported by NSF REU grant PHY-2349677.

[1] C. B. Kimmel, W. W. Ballard, S. R. Kimmel, B. Ullmann, and T. F. Schilling. Stages of embryonic development of the zebrafish. *Developmental Dynamics*, 203(3):253–310, 1995.

[2] Sebastian J. Streichan, Matthew F. Lefebvre, Nicholas Noll, Eric F. Wieschaus, and Boris I. Shraiman. Global morphogenetic flow is accurately predicted by the spatial distribution of myosin motors. *eLife*, 7:e27454, 2018.

[3] Edward M. De Robertis, Wolfgang Driever, and Roberto Mayor. Celebrating the centennial of the most famous experiment in embryology: Hilde mangold, hans spemann and the organizer. *Cells & Development*, 178:203921, 2024.

[4] Gopi Shah, Konstantin Thierbach, Benjamin Schmid, Jens Waschke, Anna Reade, Mario Hlawitschka, Ingo Roeder, Nico Scherf, and Jan Huisken. Multi-scale imaging and analysis identify pan-embryo cell dynamics of germlayer formation in zebrafish. *Nature Communications*, 10(1):5753, 2019.

[5] R. M. Warga and C. B. Kimmel. Cell movements during epiboly and gastrulation in zebrafish. *Development*, 108(4):569–580, 1990.

[6] C. Yin, M. Kiskowski, P. A. Pouille, E. Farge, and L. Solnica-Krezel. Cooperation of polarized cell intercalations drives convergence and extension of presomitic mesoderm during zebrafish gastrulation. *Journal of Cell Biology*, 180(1):221–232, 2008.

[7] M. Behrndt, G. Salbreux, P. Campinho, R. Hauschild, F. Oswald, J. Röensch, S. W. Grill, and C.-P. Heisenberg. Forces driving epithelial spreading in zebrafish gastrulation. *Science*, 338(6104):257–260, 2012.

[8] Michael Murrell, Patrick W. Oakes, Martin Lenz, and Margaret L. Gardel. Forcing cells into shape: the mechanics of actomyosin contractility. *Nature Reviews Molecular Cell Biology*, 16(8):486–498, 2015.

[9] Karsten Kruse, Jean-François Joanny, Frank Jülicher, Jacques Prost, and Ken Sekimoto. Generic theory of active polar gels: a paradigm for cytoskeletal dynamics. *The European Physical Journal E*, 16(1):5–16, 2005.

[10] Florence Serwane, Andrea Mongera, Payam Rowghanian, Daniel A. Kealhofer, Amanda A. Lucio, Zachary M. Hockenbery, and Otger Campàs. In vivo quantification of spatially varying mechanical properties in developing tissues. *Nature Methods*, 14(2):181–186, 2017.

[11] Adam C. Martin, Michael Gelbart, Rodrigo Fernandez-Gonzalez, Matthias Kaschube, and Eric F. Wieschaus. Integration of contractile forces during tissue invagination. *Journal of Cell Biology*, 188(5):735–749, 2010.

[12] George B. Arfken, Hans J. Weber, and Frank E. Harris. *Mathematical Methods for Physicists*. Academic Press, 6th edition, 2005.

[13] Srivathsan R. Naganathan and Magdalena C. Behrndt. Self-organization of zebrafish mesoderm in the absence of graded nodal signaling. *Current Biology*, 34(5):991–1002.e3, 2024.